

# Unveiling the Nature of an X-ray flare from 3XMM\* J014528.9+610729: A candidate spiral galaxy

Himali Bhatt<sup>1</sup>†, Subir Bhattacharyya<sup>1</sup>, Nilay Bhatt<sup>1</sup>, J. C. Pandey<sup>2</sup>

<sup>1</sup>*Astrophysical Sciences Division, Bhabha Atomic Research Centre, Trombay, Mumbai 400 085, India*

<sup>2</sup>*Aryabhata Research Institute of observational sciencES, Manora Peak, Nainital 263 129, India*

5 April 2018

## ABSTRACT

We report an X-ray flare from 3XMM J014528.9+610729, serendipitously detected during the observation of the open star cluster NGC 663. The colour-colour space technique using optical and infrared data reveals the X-ray source as a candidate spiral galaxy. The flare shows fast rise and exponential decay shape with a ratio of the peak and the quiescent count rates of  $\sim 60$  and duration of  $\sim 5.4$  ks. The spectrum during the flaring state is well fitted with a combination of thermal (APEC) model with a plasma temperature of  $1.3 \pm 0.1$  keV and non-thermal (POWER-LAW) model with power-law index of  $1.9 \pm 0.2$ . However, no firm conclusion can be made for the spectrum during the quiescent state. The temporal behavior, plasma temperature and spectral evolution during flare suggest that the flare from 3XMM J014528.9+610729 can not be associated with tidal disruption events.

**Key words:** X-ray flare, spiral galaxy, Tidal disruption, individual: 3XMM J014528.9+610729

## 1 INTRODUCTION

The X-ray emission from normal galaxies is mainly associated with bright high-mass X-ray binaries (HMXBs), Supernova remnants (SNRs), O-type stars and hot gas heated by energy originated in supernova explosions (Persic & Rephaeli 2002; Fabbiano 2006). The hard X-ray (2-10 keV) emission is dominated by HMXBs, and the soft X-ray (0.3-2.0 keV) emission is mostly produced by the gas at  $kT \sim 0.3$ -0.7 keV (Pereira-Santaella et al. 2011). Giant X-ray outbursts with flare peak to quiescent state flux ratio up to a factor  $\sim 200$  from non-active galaxies have also been detected with extreme X-ray softness, e.g., NGC 5905, RXJ1242-11, RXJ1624+75, RXJ1420+53, RXJ1331-32 (Komossa & Dahlem 2001). Tidal disruption of a star by a supermassive black hole (SMBHs) in the nuclei of galaxies is considered as the favoured explanation for these unusual events (e.g., Rees 1988). Based on a luminous flare seen in soft X-rays, several candidate tidal disruption events (TDE) have been identified so far (e.g., Rees 1988; Greiner et al. 2000; Esquej et al. 2007; Cappelluti et al. 2009; Saxton et al. 2012). These events

show high peak luminosities (up to  $\sim 10^{44}$  erg s<sup>-1</sup>), very soft spectra characterized by thermal emission in energy range 0.04-0.1 keV and the X-ray flux fall over the long-term as  $t^{-5/3}$  (see Komossa 2002). Komossa & Bade (1999) discussed the possibility of such outburst in a non-active galaxy due to accretion disk instability. A localized instability in an advection dominated disk can lead to such outbursts from a non-active galaxy. Therefore, X-ray outbursts from non-active galaxies provide important information on the presence of SMBHs in these galaxies and the link between active and normal galaxies (Komossa & Dahlem 2001).

In this paper, we analyzed an X-ray flare detected from an X-ray source during the X-ray observation of the open cluster NGC 663 from XMM-NEWTON (Bhatt et al. 2013, 2014). This source is given in 3XMM-DR4 catalogue as 3XMM J014528.9+610729, which is the sixth publicly released XMM-NEWTON X-ray source catalogue produced by the XMM Survey Science Centre. We made an attempt to classify this source using multiwavelength data and it has been argued that the source is a candidate spiral galaxy. We describe the X-ray data reduction procedure and information of the multiwavelength data used in the present study in §2. The identification methods of the X-ray source using multiwavelength data are given in §3. In §4, we present the temporal and spectral analysis of the X-ray data. Finally, we discussed our results in §5 and draw the conclusions in §6.

\* Based on observations obtained with XMM-NEWTON, an ESA science mission with instruments and contributions directly funded by ESA Member States and NASA

† mshimali@gmail.com

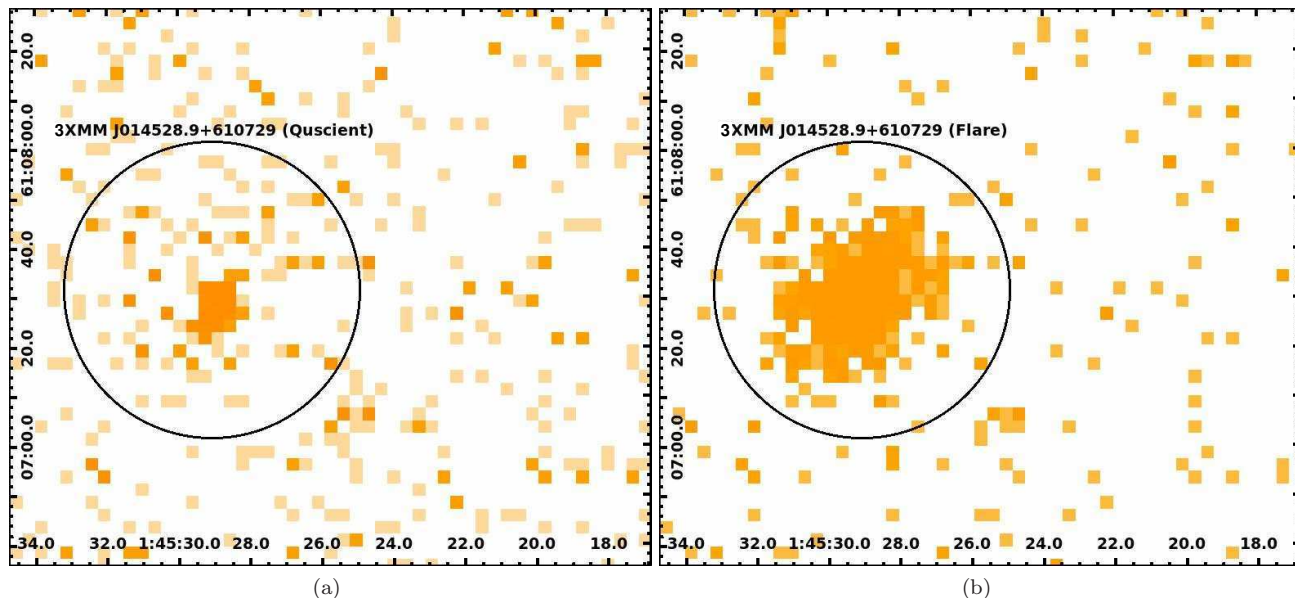


**Figure 1.** X-ray image of 3XMM J014528.9+610729. (a) before the flaring event and (b) during the flaring event. X-axis and Y-axis are representing RA(J2000) and DEC(J2000), respectively.

## 2 OBSERVATIONS AND DATA REDUCTION

3XMM J014528.9+610729 is serendipitously observed by XMM-NEWTON during the observation of the young open cluster NGC 663 on 14<sup>th</sup> January 2004 at 22:23:02 UT (53018.93266 MJD) corresponding to observation identification number 0201160101. The data obtained in the XMM-NEWTON observations have been reduced using the Science Analysis Software (SAS; Gabriel et al. 2004) version 12.0.1. The standard procedure adopted for the reduction of European Photon Imaging Camera (EPIC) and Optical Monitor (OM) data are given below. The data from the Reflection Grating Spectrometer (RGS; Brinkman et al. 1998; den Herder et al. 2001) have not been used in the present study because the X-ray source is  $\sim 9'$  away from the center of the field of view of RGS<sup>1</sup> (FOV $\sim 5'$ ) during observations.

### 2.1 EPIC data

EPIC constitutes the PN CCD detector (Strüder et al. 2001), and the twin CCD detectors MOS1 and MOS2 (Turner et al. 2001). EPIC was used in full frame mode during observations with Medium filter for an exposure time of  $\sim 42$  ks. Calibrated event files were created using SAS tasks EPCHAIN and EMCHAIN for PN and MOS detectors, respectively. The images and lightcurves of the event list were extracted using the SAS task EVSELECT. The high background periods were excluded from the observations where the total count rate (for single events of energy above 10 keV) in the instruments exceeds 0.35 and 1.0 counts  $s^{-1}$  for the MOS and PN detectors, respectively. The sums of good time intervals were found to be 32.59 ks, 33.13 ks and 28.69 ks for PN, MOS1 and MOS2 detectors, respectively. The detail description of the data reduction procedure

is given in Bhatt et al. (2013). Further, we selected single and double pixel events (corresponding to PATTERN  $\leq 4$ ) for PN and all valid events for MOS (PATTERN = 0–12). The FLAG==0 was then used for selection of events for both PN and MOS cameras. The resultant events were used for the extraction of source image, source and background lightcurves and spectra. The images of the X-ray source 3XMM J014528.9+610729 in the energy band 0.3–10.0 keV during quiescent and flaring states are shown in Figure 1. The circular region with radius  $24''$  around the source 3XMM J014528.9+610729 was used for lightcurve and spectrum extraction. The background was taken locally from identical (equal area) circular region located on the same CCD where the source was positioned for both PN and MOS detectors. The background region was selected in this way to avoid inclusion of bad pixels.

### 2.2 OM data

OM is a  $f/12.7$  Ritchey Chretien telescope coaligned with the X-ray telescopes and operating simultaneously with them (for details see Mason et al. 2001). The OM was configured in imaging mode, by using V filter<sup>2</sup> ( $\lambda_{eff} \sim 5430$  Å;  $\Delta\lambda \sim 70$  Å) during observations. Eight exposures were taken with integration time of 1748 s for each of first seven exposures (S006-S012) and 2798 s for the last one (S013). The OM covers the central  $17' \times 17'$  region of the X-ray field of view during all the exposure intervals except for S011 ( $4' \times 17'$ ). The images, source lists and magnitudes of the sources were produced by the SAS tool OMICHAIN.

<sup>1</sup> [http://XMM.esac.esa.int/external/XMM\\_user\\_support/documentation/uhb/rgs.html](http://XMM.esac.esa.int/external/XMM_user_support/documentation/uhb/rgs.html)

<sup>2</sup> [http://XMM.esac.esa.int/external/XMM\\_user\\_support/documentation/uhb/omfilters.html](http://XMM.esac.esa.int/external/XMM_user_support/documentation/uhb/omfilters.html)

### 2.3 Multiwavelength archival data

Multiwavelength data were used for source identification as the spectral class and type of the source has not yet been derived. The data from the following surveys have been used to classify the source.

#### 2.3.1 Optical data : SDSS

The optical data from the Sloan Digital Sky Survey (SDSS; Abazajian et al. 2009) have been used in the present study. The SDSS uses a dedicated wide-field 2.5 m telescope (Gunn et al. 2006) located at Apache Point Observatory (APO) near Sacramento Peak in Southern New Mexico. The SDSS photometric systems (Fukugita et al. 1996)  $u'$  (3543Å;  $\delta\lambda \sim 567\text{Å}$ ),  $g'$  (4770Å;  $\delta\lambda \sim 1387\text{Å}$ ),  $r'$  (6231Å;  $\delta\lambda \sim 1373\text{Å}$ ),  $i'$  (7625Å;  $\delta\lambda \sim 1526\text{Å}$ ) and  $z'$  (9134Å;  $\delta\lambda \sim 950\text{Å}$ ), are similar to the AB system (Oke & Gunn 1983). By matching the position of the X-ray source 3XMM J014528.9+610729 with the position of the optical sources in SDSS catalog, the optical source J014528.91+610729.5 is found to be the closest to the X-ray source 3XMM J014528.9+610729 with an offset of  $0.003''$ . The magnitudes of the optical source SDSSJ014528.91+610729.5 in SDSS bands are given in Table 1.

#### 2.3.2 Near-Infrared data: 2MASS

The Near -Infrared (NIR) data were taken from the Two Micron All Sky Survey (2MASS; Cutri et al. 2003) in  $J$  (1.25  $\mu\text{m}$ ),  $H$  (1.65  $\mu\text{m}$ ) and  $K_s$  (2.17  $\mu\text{m}$ ) bands. The cross-correlation of the position of X-ray source 3XMM J014528.9+610729 with the 2MASS catalog shows that the 2MASS source 2MASSJ01452893+6107292 is closest to the 3XMM J014528.9+610729 with an offset of  $0.324''$ , and its  $J$ ,  $H$  and  $K_s$  magnitudes are listed in Table 1.

#### 2.3.3 Near and Mid Infrared data: WISE

Wide-field Infrared Survey Explorer (WISE; Wright et al. 2010) mapped the sky at 3.4, 4.6, 12, and 22  $\mu\text{m}$  (W1, W2, W3, W4) in 2010 with an angular resolution of  $6.1''$ ,  $6.4''$ ,  $6.5''$  and  $12.0''$ , respectively. The magnitudes were taken in W1, W2, W3 and W4 bands from WISE All-Sky Data Release products (Cutri & et al. 2012). The closest counterpart of 3XMM J014528.9+610729 in WISE catalog is found within an offset of  $0.626''$ , namely, WISEJ014528.93+610728.8 and its magnitudes in WISE bands are tabulated in Table 1.

## 3 SOURCE IDENTIFICATION USING MULTIWAVELENGTH DATA

The multiwavelength data are required to classify the X-ray source into the various source types - stars, galaxies, clusters, and active galactic nuclei (AGN). We have searched the X-ray source 3XMM J014528.9+610729 into SDSS, 2MASS and WISE sky surveys covering wavelength ranging from

optical to mid IR. The values of on-axis angular resolution<sup>3</sup> (FWHM on ground) are  $6.6''$ ,  $6.0''$  and  $4.5''$  for PN, MOS1 and MOS2 detectors, respectively. The nearest counterparts of the X-ray source 3XMM J014528.9+610729 are given in Table 1. We found only one counterpart of 3XMM J014528.9+610729 in each catalog within  $4.5''$  search radius, which is the best possible resolution from XMM-NEWTON. Therefore, all these multiwavelength sources, which are within an offset of  $\sim 0.7''$ , may correspond to the X-ray source 3XMM J014528.9+610729. Using the multiwavelength information of 3XMM J014528.9+610729, we opted the following procedure to classify the X-ray source.

### 3.1 Colour-colour diagrams

Fan (1999) simulated the "fundamental plane" in colour space of  $(u' - g')$ ,  $(g' - r')$ ,  $(r' - i')$  and  $(i' - z')$  for normal stars, white dwarfs (WD), halo blue horizontal branch stars (BHBs) as well as quasars (QSO) and the compact emission-line galaxies (CELGs). All four kinds of stellar objects ( stars, WD, CELs and BHBs) are distributed basically on the same plane in colour space, but quasars are located in a different plane. Therefore, these simulations are very useful to identify QSOs. The  $(u' - g')$ ,  $(g' - r')$ ,  $(r' - i')$  and  $(i' - z')$  colours are estimated to be  $2.45 \pm 0.32$  mag,  $1.51 \pm 0.05$  mag,  $1.596 \pm 0.009$  mag and  $0.0882 \pm 0.008$  mag, respectively. The X-ray source 3XMM J014528.9+610729 (see Figure A in supplementary material) is located far away from the locus of QSOs, but above the locus of stars. Therefore, we can discard the possibility of the X-ray source 3XMM J014528.9+610729 for being a QSO, however, it is very difficult to distinguish between stars and galaxies using optical SDSS data. Therefore, we have used NIR and MIR colour-colour diagrams to distinguish it from the stars.

Recently, Tu & Wang (2013) defined a  $(J - K_s)$  and  $(K_s - W3)$  colour-colour plane to distinguish asymptotic giant branch (AGB) stars from normal stars, galaxies and QSOs. The colour-colour plane provides the 1-, 2-, and 3- $\sigma$  regions of the normal stars, 1- and 2 $\sigma$  regions of the galaxies, and the QSOs. The  $(J - K_s)$  and  $(K_s - W3)$  colours of the X-ray source 3XMM J014528.9+610729 are estimated to be  $0.82 \pm 0.06$  mag and  $3.46 \pm 0.09$  mag, respectively. The X-ray source 3XMM J014528.9+610729 (see Figure B in supplementary material) lies near the region occupied by galaxies, which is outside the 3- $\sigma$  boundary of the normal stars.

Further using WISE (W1-W2) and (W2-W3) colours, Wright et al. (2010) showed the regions occupied by stars, brown dwarfs, elliptical galaxies, spiral galaxies, starburst galaxies, luminous IR galaxies (LIRGs), low-ionization nuclear emission-line regions (NLERs) galaxies, ultraluminous infrared galaxies (ULIRGs), QSOs, Seyferts and obscured AGNs. The WISE (W1-W2) and (W2-W3) colours for the X-ray source 3XMM J014528.9+610729 are found to be  $3.124 \pm 0.082$  mag and  $0.12 \pm 0.05$  mag, respectively (see Figure C in supplementary material), and is located in the region of spiral galaxies, but near the regions occupied by LIRGs. Therefore, on the basis of multiwave-

<sup>3</sup> [http://XMM.esac.esa.int/external/XMM\\_user\\_support/ documentation/uhb/onaxisxraypsf.html](http://XMM.esac.esa.int/external/XMM_user_support/documentation/uhb/onaxisxraypsf.html)

**Table 1.** Cross identification of X-ray source 3XMM J014528.9+610729 into SDSS, 2MASS and WISE sky surveys.

Survey	Name	offset (")	Band	Magnitudes (mag)	Flux <sup>†</sup> (10 <sup>-3</sup> Jy)
SDSS	J014528.91+610729.5	0.003	<i>u'</i>	22.35±0.32	2.71± 0.81
			<i>g'</i>	19.869±0.016	6.18± 0.09
			<i>r'</i>	18.354±0.008	5.32± 0.04
			<i>i'</i>	16.758±0.005	9.48± 0.04
			<i>z'</i>	15.876±0.006	10.83± 0.06
2MASS	J01452893+6107292	0.324	J	14.413±0.041	8.03± 0.30
			H	13.832±0.044	5.94± 0.24
			<i>K<sub>s</sub></i>	13.592±0.045	3.86± 0.16
WISE	J014528.93+610728.8	0.626	W1	13.377±0.030	1.84± 0.05
			W2	13.257±0.035	1.06± 0.03
			W3	10.133±0.074	3.72± 0.25
			W4	8.90±0.37	2.85± 0.98

<sup>†</sup> : These fluxes are extinction corrected (see §3.2).

length colour-colour diagrams, the X-ray source 3XMM J014528.9+610729 is very likely to be a spiral galaxy.

### 3.2 Spectral energy distribution

The reddening towards the direction of 3XMM J014528.9+610729 in *V* band is given as  $A_V = 4.522$  mag in NASA/IPAC Extragalactic Database<sup>4</sup> using Galactic extinction from Schlafly & Finkbeiner (2011). The reddening ( $A_\lambda$ ) towards the direction of 3XMM J014528.9+610729 for SDSS wavebands *u'*, *g'*, *r'*, *i'* and *z'* are given as 6.990, 5.447, 3.768, 2.800 and 2.083 mag, respectively. For 2MASS *J*, *H* and *K<sub>s</sub>* bands, the  $A_\lambda$  are given as 1.169, 0.740 and 0.498 mag, respectively. The reddening in WISE wavebands are derived using the relations given in Gandhi et al. (2011)<sup>5</sup> in W1, W2, W3 and W4 wavebands and estimated to be 0.315, 0.238, 0.307 and 0.234 mag, respectively. The spectral energy distribution (SED) of 3XMM J014528.9+610729 is shown in Figure 2.

Using the colour-colour information, we have fitted the SED of the X-ray source 3XMM J014528.9+610729 with the templates of different types of galaxies using the template fitting procedure given by Bolzonella et al. (2000, referred as Hyperz) and Assef et al. (2008, 2010). The Galaxy template from Assef et al. (2008, 2010) is best fitted with  $\chi^2$  of 11330 (dof 11), which implies that the object is outside the parameter space covered by the models. Using Hyperz template fitting procedure, the data are best fitted with the spiral galaxy (SB2) template with  $\chi^2_\nu$  of 457 (dof 11) with a fitting probability of 0%. Therefore, none of the fitting procedure is able to give an acceptable  $\chi^2$  using any of the galaxy templates. Here, we are not able to classify the source based on the template fitting procedure, and therefore we cannot determine the redshift of the X-ray source.

## 4 RESULTS

### 4.1 X-ray lightcurves

X-ray lightcurves were extracted using SAS task EVSELECT. The background lightcurves from adjacent source-free regions were also accounted for and the background scaling factors were calculated using BACKSCALE task. To check the variation in different energy bands, the lightcurves were built in three energy bands – total (T; 0.3-10.0 keV), soft (S; 0.3-2.0 keV) and hard (H, 2.0-10.0 keV) with a time binwidth of 800 s. The background subtracted lightcurves are shown in Figure 3 for the total energy band, and in Figure 4 for soft and hard energy bands. X-ray lightcurves show flaring features where flares are characterized by two or more consecutive time bins that constitute a sequence of either rising or falling count rates, corresponding to rise and decay phase of the flare. The flare regions and quiescent regions are marked by "F" and "Q" in Figure 3 by dotted lines.

$\chi^2$ -test has been performed to estimate the statistical significance of the flare-like variability in the lightcurves and the  $\chi^2$  values with a degree of freedom (dof) are given in Table 2. The values of the probabilities of variability ( $P_{\text{var}}$ ) in lightcurves for each detector have been calculated and are found to be greater than 99.999%. Fractional root mean square (rms) variability amplitudes ( $F_{\text{var}}$ ) are estimated to quantify the amplitude of variability in the X-ray lightcurves. The  $F_{\text{var}}$  has been defined as (Edelson et al. 2002, 1990)

$$F_{\text{var}} = \frac{1}{\langle X \rangle} \sqrt{S^2 - \langle \sigma_{\text{err}}^2 \rangle} \quad (1)$$

$$\sigma_{F_{\text{var}}} = \frac{1}{F_{\text{var}}} \sqrt{\frac{1}{2N} \frac{S^2}{\langle X \rangle^2}} \quad (2)$$

where  $S^2$  is the total variance of the lightcurve,  $\langle \sigma_{\text{err}}^2 \rangle$  is the mean error squared,  $\langle X \rangle$  is the mean count rate and  $\sigma_{F_{\text{var}}}$  is the error in  $F_{\text{var}}$ . The values of  $F_{\text{var}}$  and corresponding errors are given in Table 2.

In energy band T, the mean count rates during qui-

<sup>4</sup> <http://ned.ipac.caltech.edu/>

<sup>5</sup>  $A_{W1} = 0.0697 \times A_\lambda$ ,  $A_{W2} = 0.0527 \times A_\lambda$ ,  $A_{W3} = 0.068 \times A_\lambda$ ,  $A_{W4} = 0.0517 \times A_\lambda$

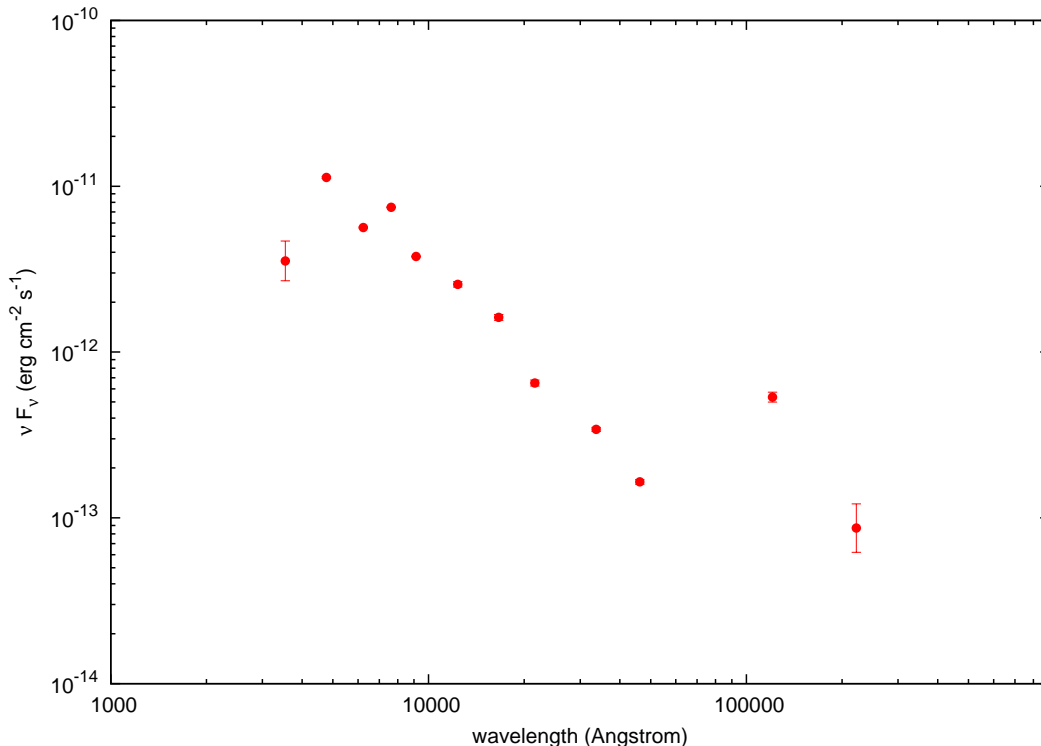


**Figure 2.** Extinction corrected observed frame spectral energy distribution of 3XMM J014528.9+610729. The Vertical error bars show  $1\sigma$  uncertainties due to photometric uncertainties on the fluxes.

**Table 2.** Timing analysis using  $\chi^2$ -test with the probabilities of rejection of the null hypothesis ( $P_{\text{var}}$ ) with dof in different energy bands– Total (T, 0.3-10.0 keV), Soft (S, 0.3-2.0 keV) and Hard (H, 2.0-10.0 keV), for each EPIC detectors. The amplitude of variability in the X-ray lightcurves is defined using  $F_{\text{var}}$ .

Energy	$\chi^2$ -Test [ $\chi^2$ (dof)]			Variability amplitude ( $F_{\text{var}}$ )		
	PN	MOS1	MOS2	PN	MOS1	MOS2
T	1944(34)	461(36)	828(40)	$2.09 \pm 0.25$	$2.06 \pm 0.25$	$2.26 \pm 0.25$
S	1947(32)	508(29)	815(39)	$2.03 \pm 0.25$	$1.79 \pm 0.24$	$2.26 \pm 0.26$
H	97(31)	67(27)	58(26)	$1.73 \pm 0.23$	$1.65 \pm 0.25$	$1.32 \pm 0.21$

escent state are estimated to be  $0.003 \pm 0.002$ ,  $0.002 \pm 0.001$  and  $0.002 \pm 0.001$  counts  $\text{s}^{-1}$  in PN, MOS1 and MOS2 detectors, respectively. The duration of the X-ray flare is  $\sim 5.6$  ks, with rise and decay times  $\sim 1.6$  ks and  $\sim 4.0$  ks, respectively. It shows a rapid rise and slower decay in count rates, and the peak count rates at flaring state are found to be nearly  $73 \pm 50$ ,  $50 \pm 25$  and  $65 \pm 34$  times more than that of the quiescent state in PN, MOS1 and MOS2 detectors, respectively.

The X-ray flare from the candidate spiral galaxy 3XMM J014528.9+610729 appears highly asymmetric with fast rise time and long decay. The decay time scales of the flares are very important to understand the physical mechanism of generation of flares. The X-ray flares from the quiescent galaxies are mainly associated with the TDEs and the flux decay of TDE flares is broadly consistent with a power law with a slope of  $\sim -5/3$  (e.g., Rees 1988; Greiner et al. 2000; Esquej et al. 2007; Cappelluti et al. 2009; Saxton et al. 2012). However, the X-ray flares from AGNs are having fast rise and exponential decay (FRED) shape (e.g., Maraschi et al. 1999; Fossati et al. 2000a). Therefore, to understand the behaviour of the flare, we have

fitted the count rate  $c(t)$  as a function of time  $t$  during the decay phase in lightcurves of PN detector with power law decay and exponential decay using the following equations, respectively.

$$c(t) = a \times t^{-\alpha} + b \quad (3)$$

where  $a$  and  $b$  are constants and  $\alpha$  is the power-law index. The decay phase is not well fitted with a POWER-LAW model as suggested by  $\chi^2_{\nu}$  value of 14.6 with dof 5.

$$c(t) = A_0 \exp^{-[(t-t_0)/\tau_d]} + q \quad (4)$$

where  $t_0$  is the time of peak count rate,  $q$  is the count rate in the quiescent state ( $0.003$  counts  $\text{s}^{-1}$ ),  $\tau_d$  is the decay time of the flare and  $A_0$  is the count rate at flare peak. The best-fit values of  $\tau_d$  is estimated to be  $1707 \pm 144$  s with  $\chi^2_{\nu}$  of 1.48 with dof 6. Thus, the flare is well fitted with the FRED shape.

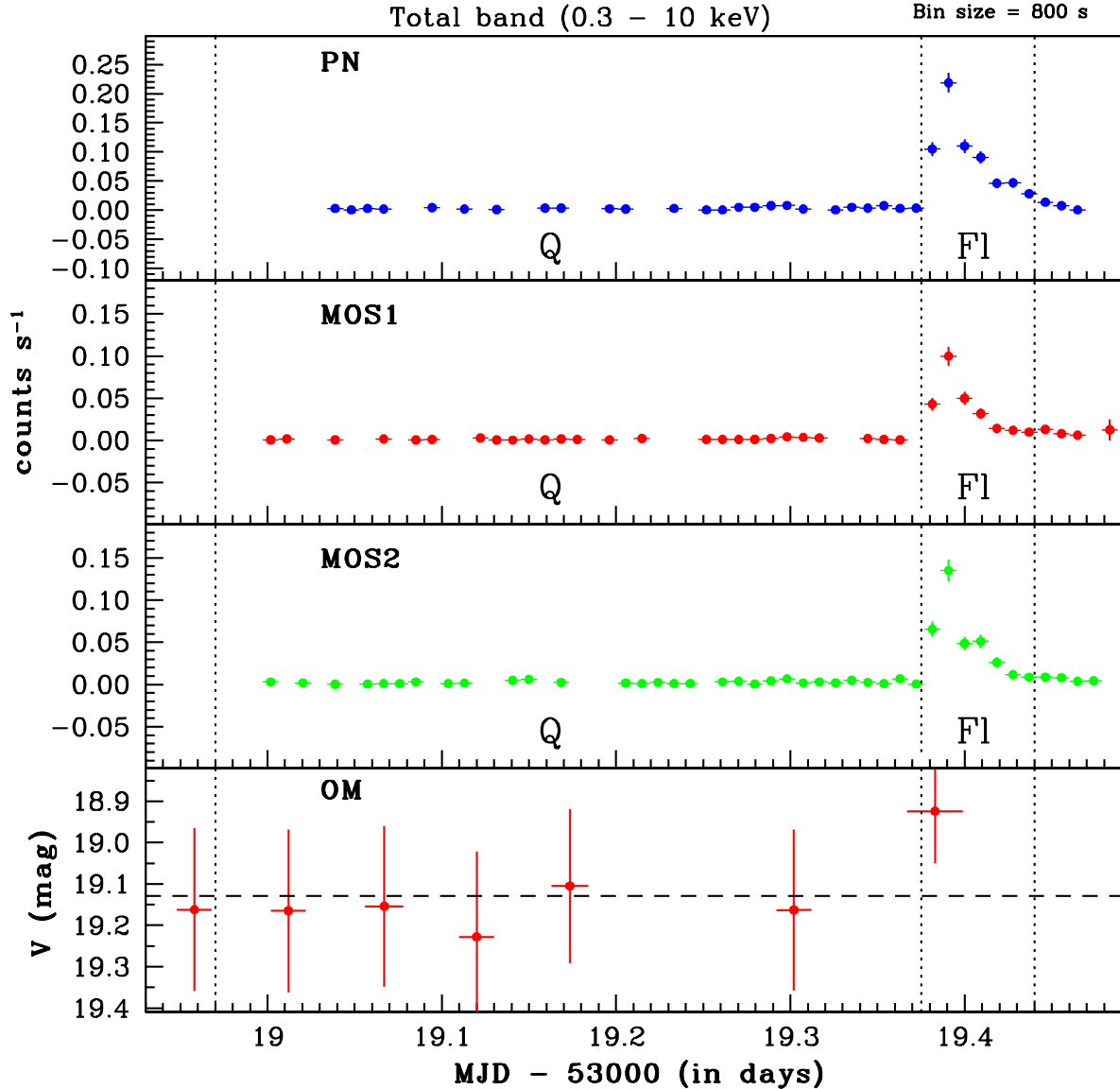


**Figure 3.** Background corrected lightcurves in EPIC (energy band 0.3 - 10 keV) and OM detectors. Quiescent states (Q) and Flaring states (Fl) are marked by dotted line in each panel.

#### 4.2 Optical lightcurve

The optical V-band magnitudes of 3XMM J014528.9+610729 for each exposure time are plotted in the lower panel of Figure 4, where dashed line represents the mean V-band magnitude of 3XMM J014528.9+610729. The flare and quiescent state regions of X-ray flare are shown by dotted lines. The flux in V-band show small enhancement during the flare, however the enhancement is within  $2\sigma$  significance level due to the large uncertainties in V-band magnitudes.

#### 4.3 X-ray Spectra

The X-ray spectra for the flaring state "Fl" and the quiescent state "Q" were generated independently in the total

energy band. The photon redistribution as well as the ancillary matrices were computed using the SAS task RMFGEN and ARFGEN. The data from MOS1 and MOS2 CCDs were combined using HEASOFT<sup>6</sup> task ADDSPEC. The PN and combined MOS spectra were rebinned to have at least 20 counts per bin. The spectra in the flaring state and the quiescent state were fitted with three different models – (a) non-thermal, (b) thermal and (c) combination of thermal and non-thermal models. The thermal model Astrophysical Plasma Emission Code (APEC) version 1.10 modeled by Smith et al. (2001) and the non-thermal POWER-LAW model are used for global fitting of X-ray spectra. The Galactic photoelectric absorption of X-rays was accounted for by using a multiplicative

<sup>6</sup> <http://heasarc.gsfc.nasa.gov/lheasoft>

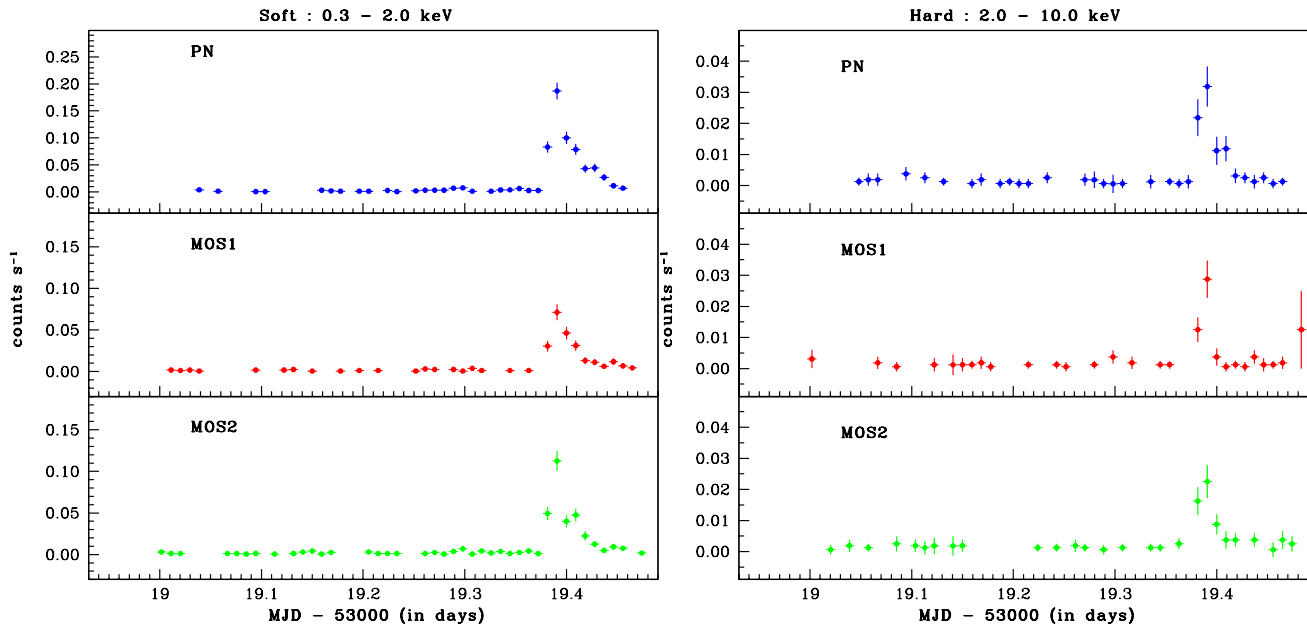


**Figure 4.** Background corrected lightcurves in EPIC detectors in energy bands *left* : soft band– S (0.3 - 2.0 keV) and *right* : hard band–H (2.0 - 10.0 KeV).

model PHABS in XSPEC (Balucinska-Church & McCammon 1992). The spectra in PN and MOS detectors were fitted simultaneously. The relative cross-calibration of PN and MOS detectors was taken care by introducing a floating normalization constant in the model during the fitting process. The best fit parameters of POWER-LAW model, APEC model and combined (APEC + POWER-LAW) model are derived using  $\chi^2$ -minimization technique in XSPEC version 12.8.0 and given in Table 3. The X-ray spectra with best-fitted models are shown in Figure 5 for the quiescent and the flaring states. Due to poor count statistics, we could not fit the Combined (APEC + POWER-LAW) model during the quiescent state.

The hydrogen column density,  $N_H$ , along the line of sight of the X-ray source is estimated to be  $6.7 \pm 1.2 \times 10^{21} \text{ cm}^{-2}$  using HEASOFT TOOL<sup>7</sup> (LAB map; Kalberla et al. 2005) with cone radius of 1 degree. We can not constrain other parameters in spectral fitting while freezing the value of  $N_H$  with  $6.7 \pm 1.2 \times 10^{21} \text{ cm}^{-2}$  in quiescent as well as flaring states. Therefore, we used  $N_H$  as a free parameter during spectral fitting. Using POWER-LAW model, the best fitted values of  $N_H$  were found to be  $> 5.0 \times 10^{21} \text{ cm}^{-2}$  and  $1.4^{+0.4}_{-0.3} \times 10^{21} \text{ cm}^{-2}$  for quiescent and flaring states, respectively. Using APEC model, the best fit values of  $N_H$  were found to be  $4.8^{+1.5}_{-1.8} \times 10^{21} \text{ cm}^{-2}$  and  $> 5.0 \times 10^{21} \text{ cm}^{-2}$  for the quiescent and the flaring states, respectively. These values of  $N_H$  are nearly similar to that of estimated with LAB map within  $2\sigma$  limits, however, it is lower during the flaring state with POWER-LAW model.

The value of  $kT$  were derived to be  $0.54^{+0.13}_{-0.17} \text{ keV}$  and  $3.18^{+0.31}_{-0.29} \text{ keV}$  during quiescent and flaring states, respectively. The best fit values of power-law indices were estimated to be  $2.27^{+0.45}_{-0.37}$  and  $2.49^{+0.19}_{-0.18}$  for the quiescent and the flaring states, respectively. As the possible mechanism of the flare is not known, we have also fitted the flare spectrum by

APEC+POWERLAW model. This gave a relatively lower temperature ( $1.33^{+0.20}_{-0.09} \text{ keV}$ ) of the thermal plasma and harder power-law index ( $1.93^{+0.24}_{-0.23}$ ) as compared to what was obtained with the POWER-LAW model only (see Table 3). The  $\chi^2_\nu$  was improved significantly while fitting the spectra with the combined (APEC+POWERLAW) model.

## 5 DISCUSSION

An X-ray flare has been detected from 3XMM J014528.9+610729 during the observations of star cluster NGC 663 by XMM-NEWTON. The colour-colour diagrams are powerful diagnostic tools in such cases where no spectroscopic information about of the sources is known. The location of the X-ray source 3XMM J014528.9+610729 in the colour-colour plane is used to identify the X-ray source in optical and infrared bands. On the basis of the optical colour-colour diagram, the possibility of the source for being a QSO is ruled out. Comparing the near and mid infrared properties of the source with the stars and galaxies using 2MASS and WISE data, it has been evident that the source is a candidate normal spiral galaxy. It makes the X-ray source 3XMM J014528.9+610729 very interesting to study as the flaring event from the non-active galaxies are very rare. The behavior of the X-ray flare and possible scenarios for the generation of the X-ray flare were further investigated.

As we do not know the exact mechanism and site of radiation emission, so we used phenomenological models to fit the spectra in the quiescent and the flaring states. The fitting of the quiescent state spectrum with APEC thermal model gave a temperature of  $0.54^{+0.13}_{-0.17} \text{ keV}$  of the emitting plasma, whereas the fitting with POWER-LAW model gave a power-law index of  $2.27^{+0.45}_{-0.37}$ . The value of equivalent hydrogen column density is consistent in both the cases. But the poor statistics of data in the quiescent state makes it

<sup>7</sup> <http://heasarc.gsfc.nasa.gov/cgi-bin/Tools/w3nh/>

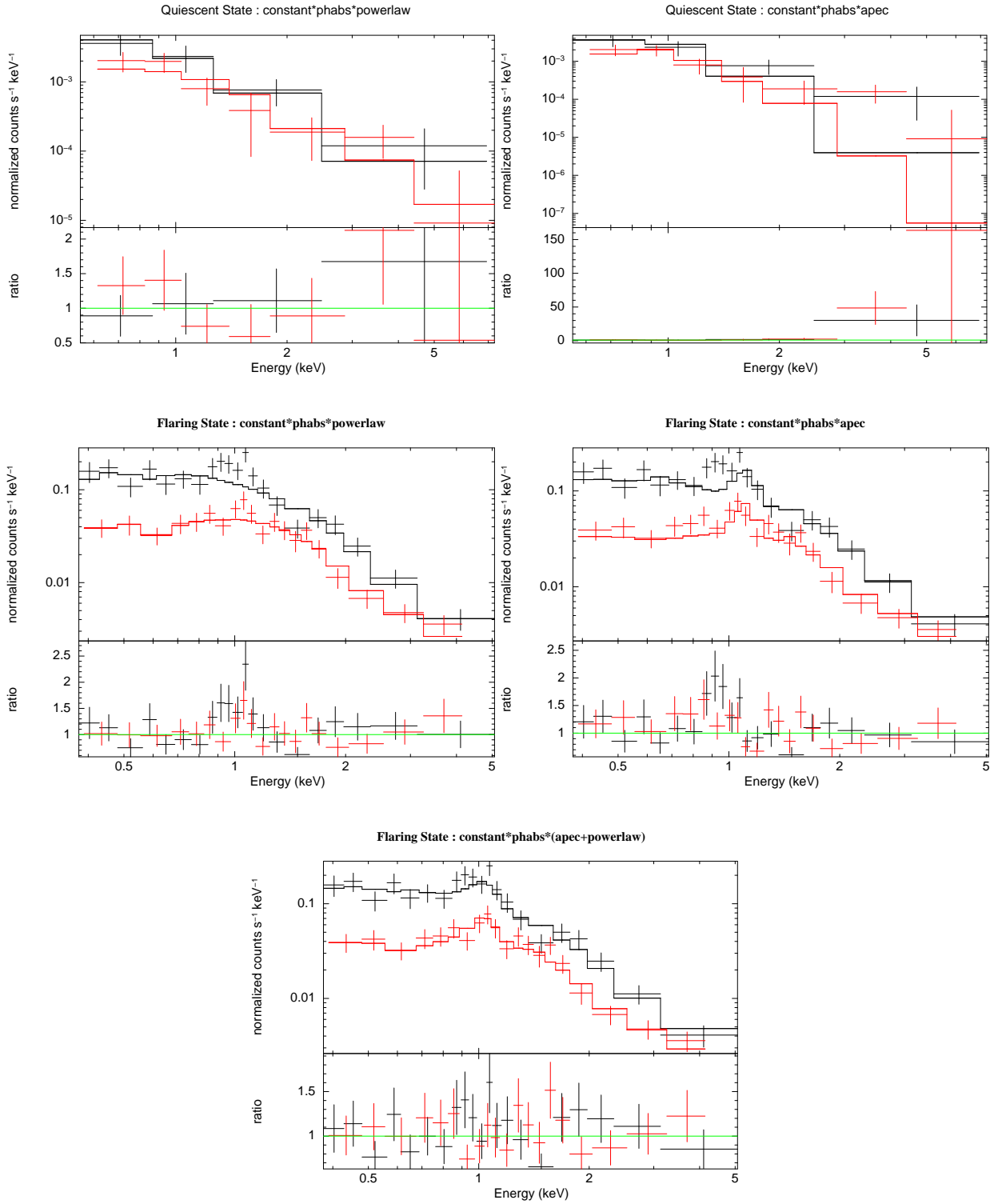


**Figure 5.** X-ray spectra in PN detector (black colour; available only in electronic form) and combined (MOS1+MOS2) spectra in MOS detector (red colour; available only in electronic form) with best-fitted models for quiescent and flaring states. The  $\chi^2$  distribution in terms of ratio are given in lower sub panels.

**Table 3.** The best fit parameters of thermal APEC and POWER-LAW model.

State	Quiescent (Q)	Flare (Fl)
Model	constant*phabs*powerlaw	
$N_H$ ( $10^{22}$ cm $^{-2}$ )	$> 0.50$	$0.14^{+0.04}_{-0.03}$
Power-law	$2.27^{+0.45}_{-0.37}$	$2.49^{+0.19}_{-0.18}$
Normalization ( $10^{-5}$ )	$0.37^{+0.08}_{-0.08}$	$25.85^{+3.96}_{-3.39}$
Constant factor	$2.02^{+0.77}_{-0.53}$	$1.47^{+0.11}_{-0.10}$
Log(Flux) (erg s $^{-1}$ cm $^{-2}$ ) [0.3-10.0 keV]	$-13.73^{+0.06}_{-0.06}$	$-11.90^{+0.01}_{-0.01}$
Log(Flux) (erg s $^{-1}$ cm $^{-2}$ ) [0.3-2.0 keV]	$-13.91^{+0.16}_{-0.25}$	$-12.03^{+0.01}_{-0.02}$
Log(Flux) (erg s $^{-1}$ cm $^{-2}$ ) [2.0-5.0 keV]	$-14.40^{+0.16}_{-0.25}$	$-12.66^{+0.01}_{-0.02}$
Log(Flux) (erg s $^{-1}$ cm $^{-2}$ ) [5.0-10.0 keV]	$-14.62^{+0.16}_{-0.25}$	$-12.96^{+0.01}_{-0.02}$
$\chi^2_\nu$ (dof)	0.66 (7)	1.30 (37)
Model	constant*phabs*apec	
$N_H$ ( $10^{22}$ cm $^{-2}$ )	$0.48^{+0.15}_{-0.18}$	$> 0.5$
kT (keV)	$0.54^{+0.13}_{-0.17}$	$3.18^{+0.31}_{-0.29}$
Normalization ( $10^{-5}$ )	$1.26^{+1.66}_{-0.67}$	$47.19^{+2.57}_{-2.56}$
Constant factor	$1.87^{+0.74}_{-0.50}$	$1.39^{+0.10}_{-0.10}$
Log(Flux) (erg s $^{-1}$ cm $^{-2}$ ) [0.3-10.0 keV]	$-13.40^{+0.06}_{-0.07}$	$-12.09^{+0.01}_{-0.01}$
Log(Flux) (erg s $^{-1}$ cm $^{-2}$ ) [0.3-2.0 keV]	$-13.40^{+0.06}_{-0.07}$	$-12.37^{+0.01}_{-0.02}$
Log(Flux) (erg s $^{-1}$ cm $^{-2}$ ) [2.0-5.0 keV]	$-15.29^{+0.07}_{-0.06}$	$-12.60^{+0.01}_{-0.02}$
Log(Flux) (erg s $^{-1}$ cm $^{-2}$ ) [5.0-10.0 keV]	$-17.81^{+0.06}_{-0.07}$	$-12.86^{+0.01}_{-0.02}$
$\chi^2_\nu$ (dof)	1.30 (7)	1.54 (37)
Model	constant*phabs*(apec+powerlaw)	
$N_H$ ( $10^{22}$ cm $^{-2}$ )		$< 0.08$
kT (keV)		$1.33^{+0.20}_{-0.09}$
Normalization (thermal; $10^{-5}$ )		$7.71^{+3.35}_{-2.05}$
Power-law		$1.93^{+0.24}_{-0.23}$
Normalization (powerlaw; $10^{-5}$ )		$13.17^{+3.34}_{-2.71}$
Constant factor		$1.43^{+0.11}_{-0.10}$
Log(Flux) (erg s $^{-1}$ cm $^{-2}$ ) [0.3-10.0 keV]		$-12.03^{+0.02}_{-0.02}$
Log(Flux) (erg s $^{-1}$ cm $^{-2}$ ) [0.3-2.0 keV]		$-12.28^{+0.01}_{-0.02}$
Log(Flux) (erg s $^{-1}$ cm $^{-2}$ ) [2.0-5.0 keV]		$-12.63^{+0.02}_{-0.02}$
Log(Flux) (erg s $^{-1}$ cm $^{-2}$ ) [5.0-10.0 keV]		$-12.77^{+0.03}_{-0.03}$
$\chi^2_\nu$ (dof)		0.93 (35)

difficult to distinguish the two models. Therefore, any further constrain can not be imposed on the quiescent state spectrum.

In case of the flaring state, we fitted the spectrum with APEC model and POWER-LAW model. The APEC model gave a temperature of  $3.18^{+0.31}_{-0.29}$  keV implying substantial heating of the plasma during the flaring process. The POWER-LAW model gave a spectral index of  $2.49^{+0.19}_{-0.18}$ . This implies that if the basic origin of radiation in the source is entirely due to some non thermal process then the spectral shape of the time averaged flare spectrum does not change much. The time averaged flare spectrum does not show significant steepening in the spectrum. The fitting of the flaring state spectrum improves when it is fitted with APEC+POWER-LAW model. In such a condition the temperature of the plasma was obtained to be  $1.33^{+0.20}_{-0.09}$  keV, which is cooler than that of obtained from APEC model only. The power-law index is found to be  $1.93^{+0.24}_{-0.23}$ , which is harder than that of obtained in the pure POWER-LAW case. Thus if it so happens that during the flare the plasma is heated and a fraction of the thermal particles of the plasma are accelerated to higher energies by some

acceleration process generating a harder spectrum, then the radiation emission can be due to some hybrid of thermal and non-thermal distribution of particles.

To have a better understanding of the flux and spectral evolution during the flare, we studied the time variation of the hardness ratio (H/S) and the hardness ratio-flux correlation. The time variation of the hardness ratio shows that the hardness reduces as the flare progresses, implying the softening of the spectrum. The hardness-flux correlation reveals a clockwise sense as the hardness evolves with the flux. Such sense actually implies that the lower energy radiation lags the higher energy emission during the radiation emission process. This kind of phenomena is observed in the case of optically thin emission from blazar jets (e.g., Kirk et al. 1998; Fossati et al. 2000b,c; Bhattacharyya et al. 2005; Zhang et al. 2006). Here, also if the radiation emission takes place in an optically thin emission region then the clockwise sense of hardness count correlation can be explained if the high energy particles are injected in the emission region within a very short time scale, and then the particles are allowed to cool by emitting radiation.

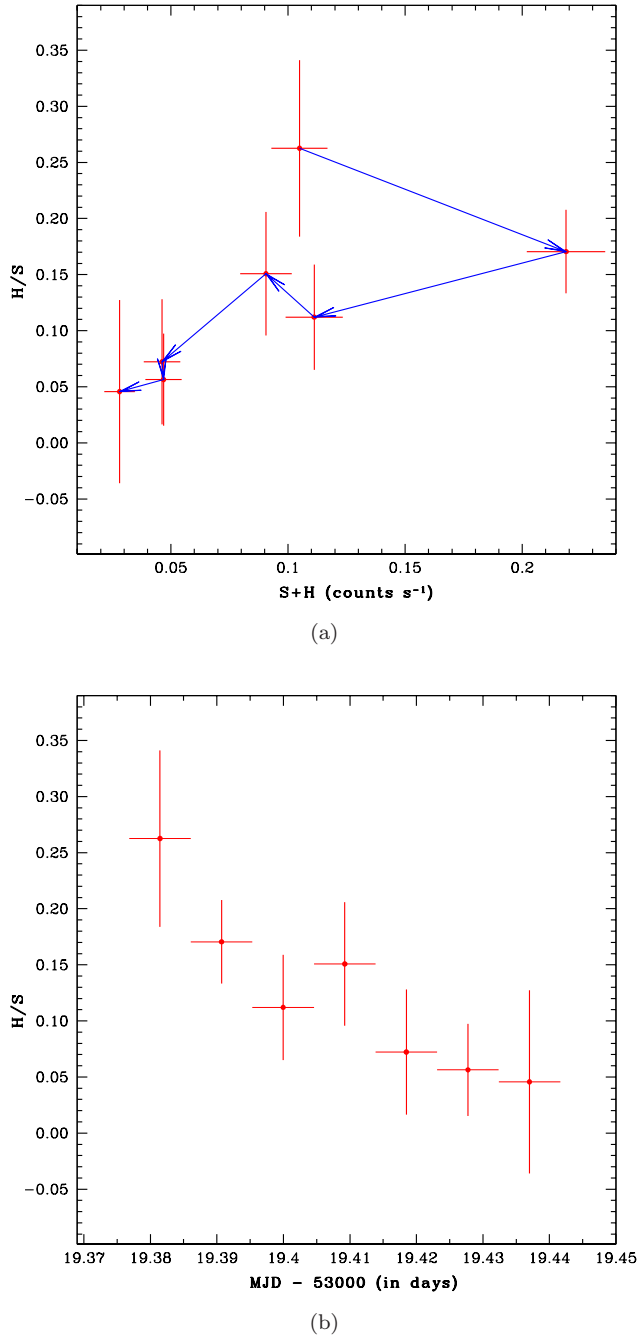


**Figure 6.** (a) Relation between hardness ratio ( $H/S$ ) and total count rates ( $H+S$ ) during the flaring state. The sense of flux evolution is shown by the arrows. (b) Evolution of hardness ratio ( $H/S$ ) during the flaring state.

The decay appears nearly exponential, therefore, it can not be associated with the flares observed due to the tidal disruption of a star by a SMBHs in the nuclei of galaxies because in such cases the flux decays with time following a power-law ( $t^{-5/3}$ ; e.g., Rees 1988; Greiner et al. 2000; Esquej et al. 2007; Cappelluti et al. 2009; Saxton et al. 2012). The thermal components which are found in the present analysis are harder compared to the component detected in the case of the flares due to the

tidal disruption of a star by a SMBHs in the nuclei of galaxies, which occurs in the temperature range 0.04-0.1 keV (for NGC 5905; Komossa 2002). However, the possibility of the X-ray source 3XMM J014528.9+610729 for being a Galactic foreground object could not be completely ruled out due to the lack of optical spectroscopic data.

## 6 CONCLUSIONS

We have detected an X-ray flare from the X-ray source 3XMM J014528.9+610729 which is serendipitously observed during the X-ray observations of the open star cluster NGC 663 from XMM-NEWTON. The identification of the X-ray source using multiwavelength data sets in optical and infrared bands has been performed, and the spectral and temporal characteristics of the source during the quiescent and the flaring states have been investigated. The main conclusions of present analysis are as follows.

- The X-ray source is found to be a candidate spiral galaxy using colour-colour information in optical, and near and mid infrared bands.
- The flare has highly asymmetrical time structure with the FRED shape, and the rise and decay times of the flare are estimated to be  $\sim 1.6$  ks and  $\sim 4.0$  ks, respectively.
- The spectrum of the source during the quiescent state is fitted with thermal APEC model and also with non-thermal POWER-LAW model. Due to the poor statistics of the data in the quiescent state no firm conclusion can be drawn regarding the nature of the source.
- In the flaring state, the spectrum can be best fitted with a spectral model combining two models (APEC+POWERLAW).
- The variation of hardness with flux indicates a clockwise structure which implies a soft lag in the emission process.
- As the specific nature of the flare mechanism is not known for a spiral galaxy, so regular monitoring of the source 3XMM J014528.9+610729 is required in X-rays and other wavebands to have an improved understanding of the source emission mechanism and link between active and normal galaxies.

## ACKNOWLEDGMENTS

Authors are thankful to Roberto J. Assef and Roser Pello for their help to use their software for fitting SED. This publication makes use of data from the Two Micron All Sky Survey, which is a joint project of the University of Massachusetts and the Infrared Processing and Analysis Center/California Institute of Technology, funded by the National Aeronautics and Space Administration and the National Science Foundation, data products from the Wide-field Infrared Survey Explorer, which is a joint project of the University of California, Los Angeles, and the Jet Propulsion Laboratory/California Institute of Technology, funded by the National Aeronautics and Space Administration and SDSS which is by the Alfred P. Sloan Foundation, the Participating Institutions, the National Science Foundation, the U.S. Department of Energy, the National Aeronautics and Space Administration, the Japanese Monbukagakusho, the Max Planck Society, and the Higher Education Funding Council for England.

Data obtained from the High Energy Astrophysics Science Archive Research Center (HEASARC), provided by NASA's Goddard Space Flight Center has also been used in the present study. HB is thankful for the financial support for this work through the INSPIRE faculty fellowship granted by the Department of Science & Technology India, and R. Koul for his support to work and to pursue DST-INSPIRE position at ApSD, BARC, Mumbai.

## REFERENCES

- Abazajian K. N. et al., 2009, *ApJS*, 182, 543  
 Assef R. J. et al., 2008, *ApJ*, 676, 286  
 Assef R. J. et al., 2010, *ApJ*, 713, 970  
 Balucinska-Church M., McCammon D., 1992, *ApJ*, 400, 699  
 Bhatt H., Pandey J. C., Singh K. P., Sagar R., Kumar B., 2013, *Journal of Astrophysics and Astronomy*, 34, 393  
 Bhatt H., Pandey J. C., Singh K. P., Sagar R., Kumar B., 2014, *Journal of Astrophysics and Astronomy*, 35, 39  
 Bhattacharyya S., Sahayanathan S., Bhatt N., 2005, *New A*, 11, 17  
 Bolzonella M., Miralles J.-M., Pelló R., 2000, *A&A*, 363, 476  
 Brinkman A. et al., 1998, in *Science with XMM*  
 Cappelluti N. et al., 2009, *A&A*, 495, L9  
 Cutri R. M., et al., 2012, *VizieR Online Data Catalog*, 2311, 0  
 Cutri R. M. et al., 2003, *VizieR Online Data Catalog*, 2246, 0  
 den Herder J. W. et al., 2001, *A&A*, 365, L7  
 Edelson R., Turner T. J., Pounds K., Vaughan S., Markowitz A., Marshall H., Dobbie P., Warwick R., 2002, *ApJ*, 568, 610  
 Edelson R. A., Krolik J. H., Pike G. F., 1990, *ApJ*, 359, 86  
 Esquej P., Saxton R. D., Freyberg M. J., Read A. M., Altieri B., Sanchez-Portal M., Hasinger G., 2007, *A&A*, 462, L49  
 Fabbiano G., 2006, *Advances in Space Research*, 38, 2937  
 Fan X., 1999, *AJ*, 117, 2528  
 Fossati G. et al., 2000a, *ApJ*, 541, 153  
 Fossati G. et al., 2000b, *ApJ*, 541, 153  
 Fossati G. et al., 2000c, *ApJ*, 541, 166  
 Fukugita M., Ichikawa T., Gunn J. E., Doi M., Shimasaku K., Schneider D. P., 1996, *AJ*, 111, 1748  
 Gabriel C. et al., 2004, in *Astronomical Society of the Pacific Conference Series*, Vol. 314, *Astronomical Data Analysis Software and Systems (ADASS) XIII*, Ochsenbein F., Allen M. G., Egret D., eds., p. 759  
 Gandhi P. et al., 2011, *ApJ*, 740, L13  
 Greiner J., Schwarz R., Zharikov S., Orio M., 2000, *A&A*, 362, L25  
 Gunn J. E. et al., 2006, *AJ*, 131, 2332  
 Kalberla P. M. W., Burton W. B., Hartmann D., Arnal E. M., Bajaja E., Morras R., Pöppel W. G. L., 2005, *A&A*, 440, 775  
 Kirk J. G., Rieger F. M., Mastichiadis A., 1998, *A&A*, 333, 452  
 Komossa S., 2002, in *Reviews in Modern Astronomy*, Vol. 15, *Reviews in Modern Astronomy*, Schielicke R. E., ed., p. 27  
 Komossa S., Bade N., 1999, *A&A*, 343, 775  
 Komossa S., Dahlem M., 2001, *ArXiv Astrophysics e-prints*  
 Maraschi L. et al., 1999, *ApJ*, 526, L81  
 Mason K. O. et al., 2001, *A&A*, 365, L36  
 Oke J. B., Gunn J. E., 1983, *ApJ*, 266, 713  
 Pereira-Santaella M. et al., 2011, *A&A*, 535, A93  
 Persic M., Rephaeli Y., 2002, *A&A*, 382, 843  
 Rees M. J., 1988, *Nature*, 333, 523  
 Saxton R. D., Read A. M., Esquej P., Komossa S., Dougherty S., Rodriguez-Pascual P., Barrado D., 2012, *A&A*, 541, A106  
 Schlafly E. F., Finkbeiner D. P., 2011, *ApJ*, 737, 103  
 Smith R. K., Brickhouse N. S., Liedahl D. A., Raymond J. C., 2001, *ApJ*, 556, L91  
 Strüder L. et al., 2001, *A&A*, 365, L18  
 Tu X., Wang Z.-X., 2013, *Research in Astronomy and Astrophysics*, 13, 323  
 Turner M. J. L. et al., 2001, *A&A*, 365, L27  
 Wright E. L. et al., 2010, *AJ*, 140, 1868  
 Zhang Y. H., Treves A., Maraschi L., Bai J. M., Liu F. K., 2006, *ApJ*, 637, 699

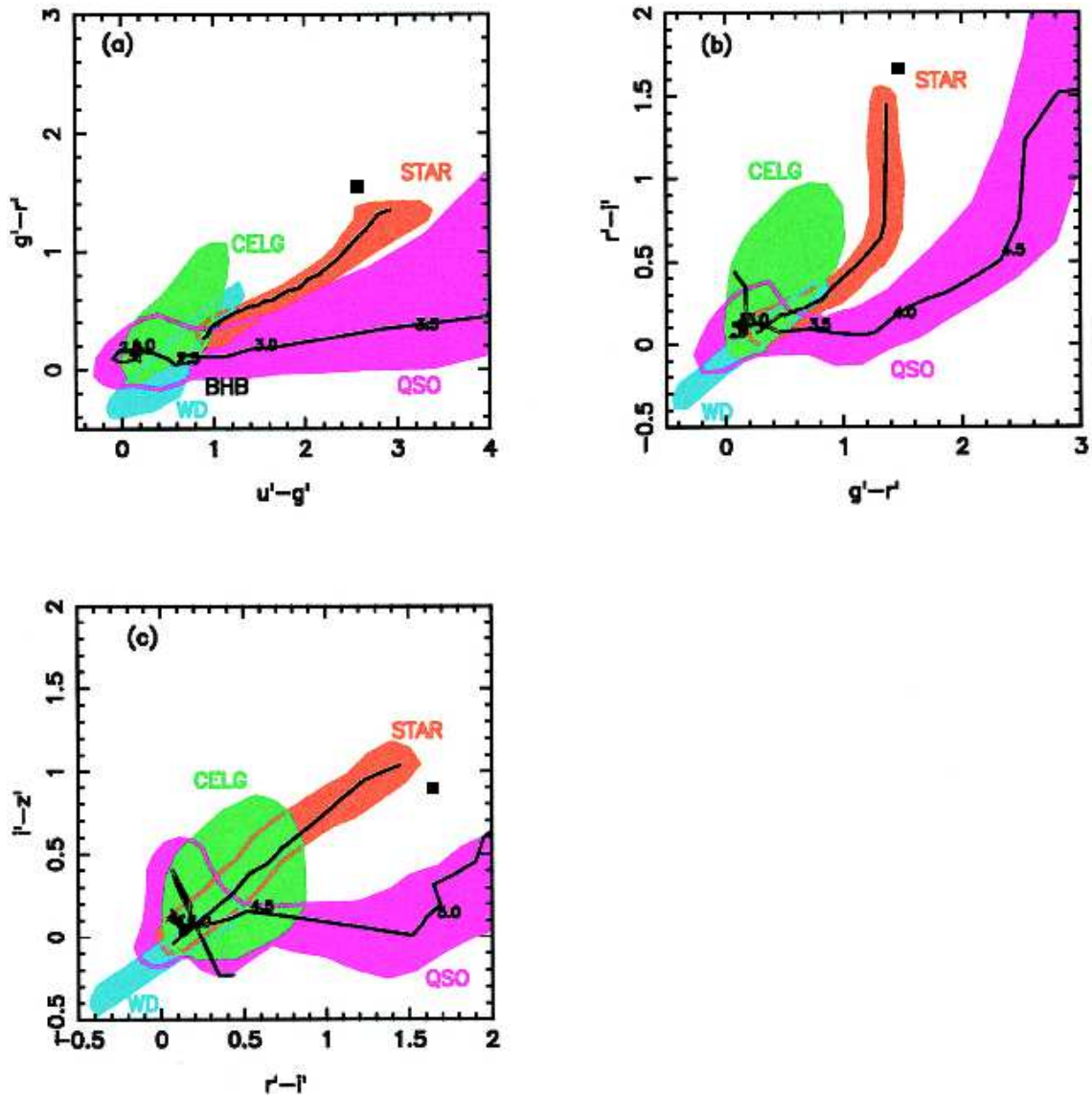


**Figure A.** Color-color diagrams from Fan (1999), (a)  $(u' - g')$  vs  $(g' - r')$ , (b)  $(g' - r')$  vs  $(r' - i')$  and (c)  $(r' - i')$  vs  $(r' - z')$ . The locations of objects with different classes: normal Galactic stars (STAR), white dwarfs (WD), quasars (QSO), compact emission-line galaxies (CELGs) and halo blue horizontal branch stars (BHBs) are shown. The solid lines going through the stellar regions are the best-fitted stellar locus points using the algorithm of Newberg & Yanny (1997). The lines going through the quasar regions are the median quasar tracks as a function of redshift. The location of 3XMM J014528.9+610729 in this color-color plane is shown by a symbol of square.

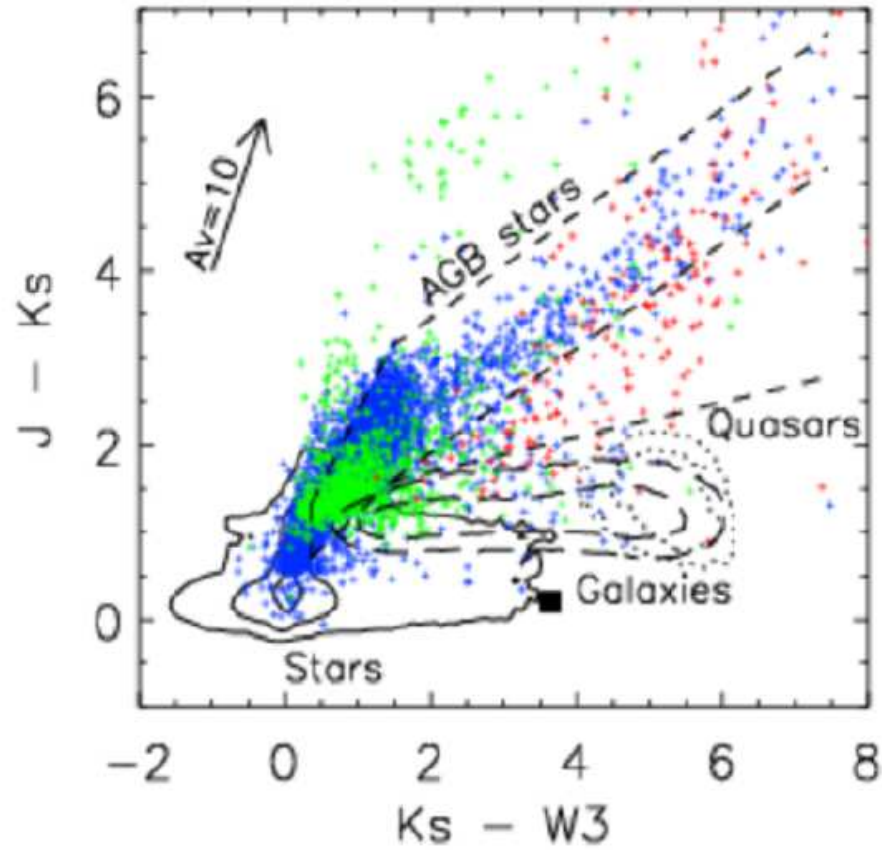


**Figure B.** Color-color diagram,  $(K_s - W3)$  vs  $(J - K_s)$  from Tu & Wang (2013). Plus symbols : blue represents C-rich AGB stars, green represents AGB stars and red represents O-rich stars. The solid contours show 1-, 2-, and 3- $\sigma$  regions of the normal stars, long-dashed contours 1- and 2- $\sigma$  regions of the galaxies, and dotted contours 1- and 2- $\sigma$  regions of the quasars. The dashed lines define the region for the AGB stars. The direction of extinction is shown by the arrow. The symbol of square represents the location of 3XMM J014528.9+610729 in color-color plane.

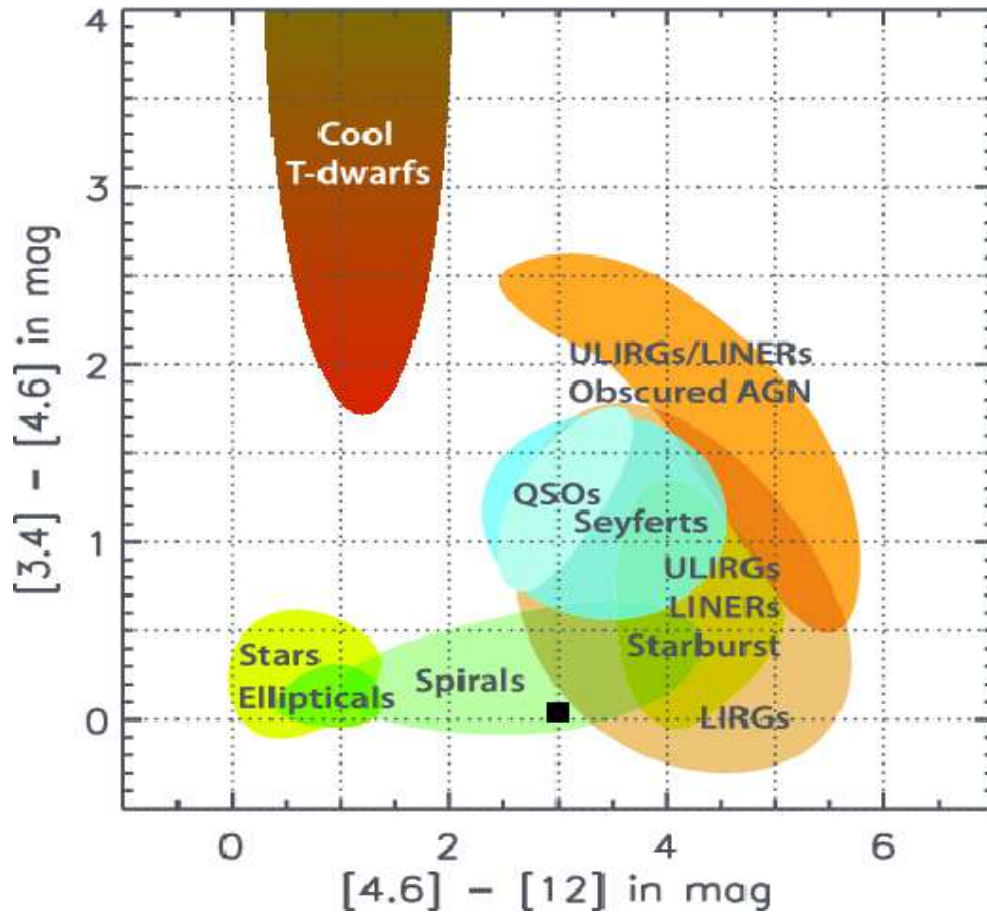


**Figure C.** Color-color diagram (W2-W3) vs (W1-W2) : figure is taken from Wright et al. (2010). , Different regions occupied in color-color plane by stars, brown dwarfs, different type of galaxies and AGNs. of 2MASS and WISE bands showing the locations of objects with different classes. The symbol of square represents the location of 3XMM J014528.9+610729 in color-color plane.